Proc. of the 5th WSEAS/IASME Int. Conf. on Electric Power Systems, High Voltages, Electric Machines, Tenerife, Spain, December 16-18, 2005 (pp156-164)

In-wheel Permanent Magnet Motors for Public Transport Application

M.ANDRIOLLO[1], G.BETTANINI[2], G.MARTINELLI[2], A.MORINI[2], S.STELLIN[2], A.TORTELLA[2]

[1] Department of Electrotechnics
Polytechnic of Milano
P.zza L. da Vinci 32, 20133 Milano
ITALY

[2] Department of Electrical Engineering
University of Padova
Via Gradenigo 6/a, 35131 Padova
ITALY

Abstract – The paper presents a methodology for the electromagnetic analysis and the design of permanent magnet in-wheel motors for the propulsion of electric buses. The methodology is applied to radial, axial and transverse flux magnetic configurations and it is able to take into account the different motor geometries as well as the design techniques for the performance evaluation. After the formulation of the constraints on the design variables, the criteria for the execution of the parametric analysis are discussed, with particular reference to the identification of an optimal configuration in terms of torque performance. Finally a non-linear mathematical model is defined to simulate the motor performance in dynamical conditions. Some significant results obtained by using the methodology are presented in the example of application.

Key-words: electric vehicles, in-wheel motors, permanent magnet machines, radial flux motors, axial flux motors, transverse flux motors, FEM analysis, dynamical analysis

1 Introduction

The increase of the air and noise pollution requires the adoption of urban transport systems with low environmental impact. An effective solution in the short-term is represented by the hybrid electric buses and in the near future by the zero-emission buses, with fuel cell and energy storage devices. In both cases the propulsion system is based on electric motors, such as the squirrel cage induction motors, coupled to the gear-box and located in the front or rear of the vehicle.

In order to overcome the gear-box drawbacks (low efficiency, frequent maintenance), an alternative solution has been recently proposed, consisting of brushless permanent magnet (PM) motors, installed inside the wheel (in-wheel motors). The rotor is directly coupled to the rim which is suspended on bearings mounted on the fixed shaft; the stator, with the ferromagnetic cores and the armature windings, is also integral with the shaft (Fig.1). The mechanical connection to the rim can occur circumferentially (Fig.1a), through one (Fig.1b) or both the lateral sides (Fig.1c): in the latter case the coupling surface is wider and the effects of accidental shocks in the vertical direction during the motion are reduced. The main advantage deriving from the use of in-wheel motors is the removal of the gearbox with the related transmission losses. The global efficiency is further increased by the absence of the field winding losses. Additional favourable features are the high torque at low speed and the high power density thanks to the adoption of rare-earth PMs. The disadvantages are the manufacturing costs, the possible PM demagnetisation at high temperatures or in short circuit conditions and the not well established operating reliability; such problems are expected to be significantly reduced in the near future, thanks to the cost-competitiveness of high energy PMs, to their better technical characteristics and to the experience gained in the large number of experimentations in progress.

In any case the design of in-wheel motors must comply with the rim diameter restrictions, achieving at the same time high torque and power density, high torque quality, high efficiency, compactness, lightness, overload capability and low noise and vibration levels.

A PM motor for direct drive applications may be realized according to different magnetic configurations and the choice depends also on the mechanical and electromagnetic constraints imposed by the kind of installation.

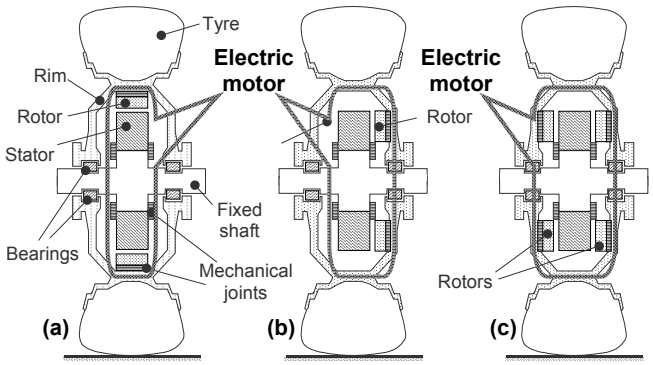

Fig.1. In-wheel motor assemblies: radial (a), single-side axial (b) and double-side axial (c) configurations.

A classification based on the flux distribution in the magnetic circuit leads to the subdivision of the PM motors into:

- radial flux PM motors (RFPM) [1÷4];
- axial flux PM motors (AFPM) [5÷16];
- transverse flux PM motors (TFPM) [17÷19].

Different manufacturing solutions can be implemented for each of them, depending on the presence of slotting (slotted or slotless configurations), on the reciprocal position between rotor and stator and on the single or multi-stage assemblies. Though the PMs are generally on the rotor surface, a radial flux configuration, called vernier hybrid motor (VHM), has the PMs placed on the surface of the stator poles [20÷23].

The several arrangements proposed for each topology and the not well established rating criteria make very troublesome the comparison of different motors, even if a particular configuration can be more convenient than others according to the specific application [24÷29].

The paper is focused on the analysis of in-wheel motors for urban buses, with surface magnet configurations (SPM motors).

2 In-wheel SPM motors

The motor configurations considered in the paper are shown in Figs.2÷6, in which the main geometric quantities are also indicated.

The radial flux motor (RFPM) with the PMs on the outer rotor is represented in Fig.2. The motor is of easy manufacturing and it is easy to improve the torque by increasing the motor depth, the diameter being equal; the torque ripple may be reduced by suitably shaping the stator teeth or by skewing the PMs.

In the axial flux motors with disc (AFPM-NS, Fig.3) and torus stator (AFPM-NN, Fig.4) [9] and in the transverse flux motor (TFPM, Fig.5) [18], the torque is exerted on two opposite lateral rotor sides (double-side configuration); in this way the axial pull due to PMs is compensated and the torque ripple may be reduced by shifting the PM arrays on the opposite rotor sides. The doubling of the phase coils in AFPM-NS and TFPM motors allows to reduce the overall size and makes the installation of the stator core easier; on the contrary, the coil assembling and wiring are laborious, particularly in many-poles configurations, even if the coil pre-installation on the stator core can lessen the difficulties. Switching from series to parallel coil connection allows to match different supply conditions and to limit the torque decrease in the high speed range, by reducing the counter e.m.f.. In the AFPM-NS motor, the stator mass can be reduced by eliminating the stator yoke, not necessary to carry the PM flux; yet, it can be necessary to join the stator to the axle. On the contrary, in the AFPM-NN motor the stator yoke cross section must be sized for the flux of both the PM arrays.

The main favourable features of the TFPM motor are the limited rotor mass, the feasibility of an effective cooling system and the possibility of torque increment by coupling several rotor modules in multiple-stack configurations [18], the same outer diameter being maintained. The main drawbacks are the difficulty in the rotor mounting and linking to the rim, the reduction of the radial space for the coils and the increase of the eddy currents (the fringing fluxes strike the sides of the transversally laminated stator cores).

All the so far considered configurations share the PM arrangement on the rotor core, in its turn linked to rim: this complicates the rotor-rim-wheel assembling and requires an accurate PM fixing.

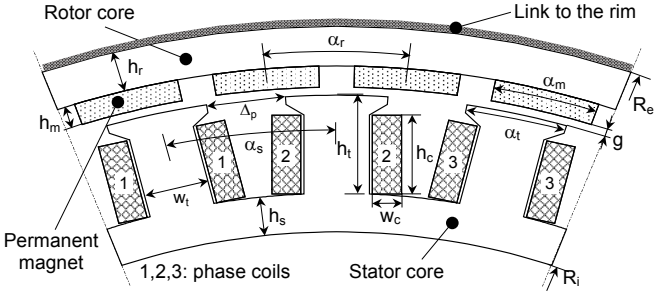

Fig.2. Radial flux PM motor (RFPM).

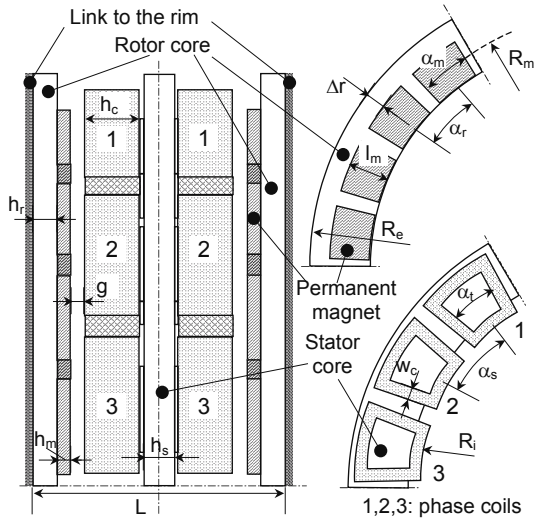

Fig.3. Axial flux PM disc motor (AFPM-NS).

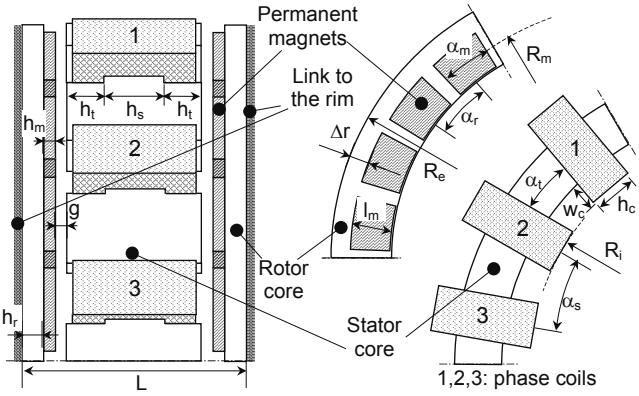

Fig.4. Axial flux PM motor with toroidal stator (AFPM-NN).

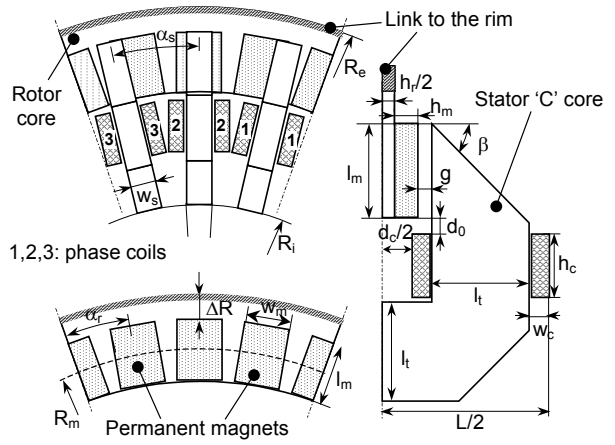

Fig.5. Transverse flux PM motor (TFPM).

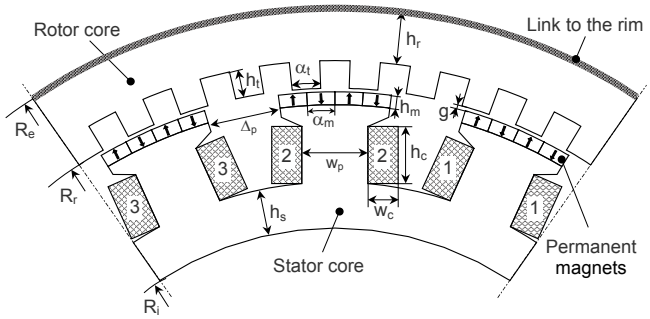

Fig.6. Radial flux vernier hybrid motor (VHM).

The VHM motor, with both the windings and the PMs on the stator (Fig.6), simplifies the manufacturing, since each pole, with the coil and the PMs, can be assembled separately and then mounted on the stator core; furthermore, the sturdiness and relative lightness of the rotor simplifies the wheel installation. On the other hand, the oscillation of the rotor flux at the supply frequency requires the core lamination, differently from the motors with rotor PMs.

The paper presents a general methodology for the design of in-wheel motors, able to take into account the different geometric structures, which heavily affect both the design constraints and the techniques for the performance estimation. At first the main geometric constraints, related to the available space inside the wheel and to the manufacturing aspects, are defined; then the procedure for the parametric analysis is described, which operates on the main design variables and makes use of a FEM code applied on suitable 2D geometrical models. Subsequently, the criteria to characterize the optimal configurations are defined, according to the output torque and to the weight of the active components, included in suitable performance indexes; in this way the capabilities of different configurations to fit the requirements can be compared. Finally, the procedure for the definition of a non linear mathematical model for each motor configuration is described: in this way the motor dynamic behaviour in steady-state running and during transients with different supply strategies can be to simulated, the dependence of the electromagnetic quantities on speed can be evaluated and the supply system specifications can be assessed. Results obtained by using the methodology are presented in the examples of application.

3 Design variables and constraints

The geometric quantities more affecting the torque performance and the weight are the tooth width w_t (or, equivalently, its angular amplitude α_t), the magnet length l_m (corresponding to the winding active length), width w_m (or its angular amplitude α_m) and height h_m. Nevertheless, the choice and the variation ranges of the design variables must take into account the geometric and electromagnetic constraints of each configuration.

As regards the geometric constraints, the overall radial size R_e is imposed by the standard rim inner radius, the minimum inner radius $R_{i,min}$ is determined by the link to the axle, the maximum axial size L_{max} is limited by the wheel clearance gauge and the air-gap width g, even if determined according to electromagnetic criteria, must comply with the manufacturing requirements and the mechanical tolerances. Furthermore, a clearance must be assured to place the forced cooling apparatus, the feeders and the rotor-rim linking.

As regards the electromagnetic constraints, the current density δ is determined by the cooling system, the maximum flux density B_{max} in the iron core is restrained to limit the magnetizing current and the iron losses, the minimum mean PM flux density $B_{m,min}$ is fixed to avoid the irreversible demagnetisation in the worst conditions, the maximum supply frequency is linked to the eddy current losses (even with relatively low angular speeds, the frequency may be several hundred Hz if the pole number is high to limit the iron weight).

The same PM volume V_m being maintained, a definite height/cross section ratio $h_m/(w_m \cdot l_m)$ maximizes the no-load PM flux, operating at the maximum PM energy product $(BH)_{max}$. However, a minimum PM height $h_{m,min}$ must be assured, to avoid the irreversible demagnetisation produced by the armature m.m.f. under the worst conditions (maximum allowable temperature and maximum short circuit current).

4 Parametric analysis

In the preliminary design, the knowledge of the influence of parametric variations on the motor performance is a crucial matter. Because of the innovative configuration of in-wheel motors and of the saturation effects, analytical or empirical design formulations are hard to be retrieved, differently from conventional motors. The availability of FEM codes for the electromagnetic analysis can somehow compensate the lack of experimental information, provided that the

use of the codes is adequately automated to vary the geometrical and electromagnetic configuration in predefined ranges. Such automated procedure should also post-process the results to obtain the significant quantities for the performance assessment.

A straightforward application of this approach may result in extremely high calculation times: a previous investigation of the electromagnetic behaviour under different load conditions is therefore convenient, if not necessary, to restrain the analysis to the most significant parameters and consequently to reduce the number of the examined sample configurations. Other techniques can be used to the same purpose, such as:

i. analysis of restricted portions of the structure, taking into account symmetries and/or periodicities of the electromagnetic configuration;
ii. definition of simplified 2D models, able to take into account also the end winding effects with acceptable accuracy;
iii. modelling of the electromagnetic configuration by means of equivalent lumped-constant magnetic circuits, to evaluate the instantaneous fluxes flowing through the various branches.

4.1 Evaluation of the torque performance

With reference to the performance evaluation, the most significant parameters are undoubtedly the torque T_{em} and its related quantities (mean value $\langle T_{em}\rangle$, ripple R_T, ratio of $\langle T_{em}\rangle$ to the mass of the motor components). Once the torque has been numerically calculated for n_r rotor positions θ, the instantaneous value of the steady-state torque $T_{em}(\theta)$ is represented by means of the truncated Fourier series expansion:

$$T_{em}(\theta) = \langle T_{em}\rangle + \sum_{k=1}^{n_h} T_k \cdot \sin(3k\, n_\tau\, \theta + \beta_k) \qquad (1)$$

with n_τ number of polar pitches; the mean value $\langle T_{em}\rangle$, the harmonic amplitude T_k and phase β_k are calculated by interpolating the 2D FEM results.

The torque ripple and the specific torques are then derived according to:

$$R_T = \sqrt{\sum_{k=1}^{n_h} T_k^2} \Big/ \langle T_{em}\rangle \qquad \sigma_i = \frac{\langle T_{em}\rangle}{m_i} \quad (i = w, S, pm, R, T) \qquad (2)$$

given the masses m_w (coils), m_S (stator), m_{pm} (magnets), m_R (rotor) and m_T (motor).

In order to match several (usually conflicting) requirements on the torque performance, it can be convenient to define a suitable global index G according to the following general formulation:

$$G = \chi_1 \cdot \frac{\langle T_{em}\rangle^*}{\langle T_{em}\rangle} + \chi_2 \cdot \frac{R_T}{R_T^*} + \sum_{i=w,S,pm,R,T} \chi_i \cdot \frac{\sigma_i^*}{\sigma_i} \qquad (3)$$

The superscript * identifies the values related to a reference configuration and the weighting normalized coefficients χ_k (k=1, 2, w, S, pm, R, T; $\Sigma_k\chi_k$=1) define the relative importance of each component. According to (3), the optimal configuration corresponds to the minimum of G.

4.2 Equivalent 2D geometrical models

In the RFPM and VHM motors (Figs.2 and 6), transversal cross-section models are effective to calculate the torque by means of 2D FEM analyses. In the AFPM and TFPM motors, 2D equivalent models can be obtained by rectifying one or more coaxial cylindrical sections with radii in the range [R_m–l_m/2, R_m+l_m/2], with R_m mean magnet radius [18] (Figs.3÷5); the torque is then evaluated by averaging the products force by radius of each section. For the AFPM motors one section at R_m generally gives adequate accuracy; for the TFPM motors at least three sections at R_m–l_m/4, R_m, R_m+l_m/4 are necessary, because of the PM shape.

Another approach consists of the modelling of the magnetic configuration by means of a lumped-constant circuit, in which each branch is represented by suitable permeances [22]. To the purpose of the torque evaluation, the identification of the air-gap permeances as functions of θ is especially relevant.

The technique can be applied in the preliminary design of rather complex configurations (such the VHM one); in this case the four pole-pitch rectified section of Fig.7 allows to evaluate the PM inner, left-side and right-side leakage and air-gap reluctances (R_{pm}, $R_{\sigma L}$, $R_{\sigma R}$ and R_g, respectively) as functions of the PM position x. The actual angular displacement is given by $\Delta\theta = \pi x/(\tau N_r)$, with N_r number of rotor teeth. By means of FEM analyses, the reluctances can be evaluated as:

$$R_{pm} = \frac{F_m - \langle \Delta U_{pm}\rangle}{A_{z1} - A_{z4}} \qquad R_g = \frac{\langle \Delta U_{pm}\rangle}{A_{z2} - A_{z3}}$$
$$R_{\sigma L} = \frac{\langle \Delta U_{pm}\rangle}{A_{z1} - A_{z2}} \qquad R_{\sigma R} = \frac{\langle \Delta U_{pm}\rangle}{A_{z3} - A_{z4}} \qquad (4)$$

where F_m is the no-load PM m.m.f., $\langle \Delta U_{pm}\rangle$ the mean value of the m.m.f. drop at the PM surface and A_{zi} (i=1,2,3,4) the magnetic potential vector value at the points P_i of Fig.7.

The instantaneous torque is then obtained as:

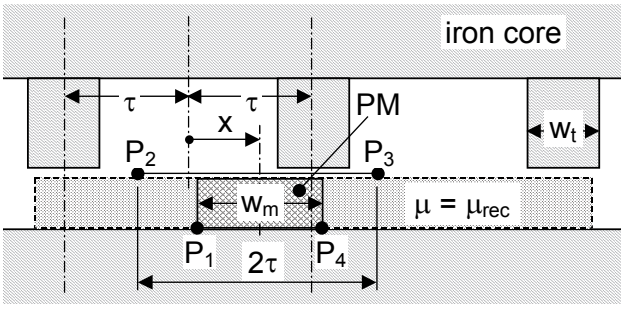

Fig.7. Rectified model for the evaluation of the air-gap and of the PM leakage reluctances for VHM (τ: PM pitch).

$$T_{em}(\theta)=\frac{1}{2}\left(\sum_{h,k=1,2,3}\partial\Lambda_{hk}/\partial\theta\cdot F_h F_k+\partial\Lambda_{mm}/\partial\theta\cdot F_m{}^2+\right.$$
$$\left.+\sum_{h=1,2,3}\partial\Lambda_{hm}/\partial\theta\cdot F_h F_m\right) \quad (5)$$

where F_h (h=1,2,3) is the phase-winding m.m.f., Λ_{hk} the mutual permeance between h and k phases (h,k=1,2,3), Λ_{hm} the mutual permeance between the h phase and the PMs and Λ_{mm} the overall PM permeance.

5 Dynamical model

The study of the motor dynamical behaviour needs the solution of the phase voltage equations $\mathbf{u}=\mathbf{R}\cdot\mathbf{i}+p\boldsymbol{\psi}$, with $\mathbf{u}=\{u_1,u_2,u_3\}$ voltages, $\mathbf{i}=\{i_1,i_2,i_3\}$ currents, $\boldsymbol{\psi}=\{\psi_1,\psi_2,\psi_3\}$ flux linkages and $\mathbf{R}=\mathrm{diag}\{r_1,r_2,r_3\}$ resistances. The flux linkage can be expressed as:

$$\psi_h(\theta,\boldsymbol{i})=\phi_{mh}(\theta,\boldsymbol{i})+\sum_{k=1}^{3}l_{hk}(\theta,\boldsymbol{i})\cdot i_k \quad (6)$$

where ϕ_{mh} is the PM contribution and l_{hk} are the winding self and mutual inductances. A non-linear mathematical model allows to obtain ψ_h as function of the currents and θ by means of analytical expressions.
The direct application of 3D FEM codes for different set of values of the currents and θ could lead to calculation overloads; alternative approaches are then convenient, such as the reduction of the number of state variables and/or the adoption of 2D simplified models.

5.1 Reduction of the state variables

A single-phase supply is assumed, with an equivalent current reproducing the effects of the mutual flux linkages with the other phases [19]. The equivalent current i_h^* is given by:

$$i_h^*=i_h+\sum_{\substack{k=1\\k\neq h}}^{3}\frac{l_{hk}}{l_{hh}}\cdot i_k=i_h+\sum_{\substack{k=1\\k\neq h}}^{3}\sigma_{hk}\cdot i_k \quad (7)$$

where i_k, are the actual currents. Since the coefficients $\sigma_{hk}=l_{hk}/l_{kk}$ depend in turn on the equivalent current, an iterative procedure is performed, with the actual current values as initial guess. Afterwards, ψ_h is got from (6) by setting the h-th element of $\mathbf{i}$ to i^*_h and the rest to 0. The quantities ϕ_{mh} and l_{hh} are sampled by means of automated sequences of 2D or 3D FEM analyses, with n_r rotor steps per pole pitch τ and n_i values of single-phase current. The sampled values are interpolated by polynomials as functions of the current and by truncated Fourier series as functions of θ.

5.2 Simplified 2D analyses

Under suitable conditions, 2D models make possible the evaluation of the instantaneous flux linkages with remarkable calculation time savings, taking anyway into account the end-winding effects; according to this, the flux linkage ψ_h may be expressed as the sum of two contributions: ψ'_h, related to the active winding parts, and ψ''_h, related to the end-winding; a relation equivalent to (6) holds for both the terms. The contribution ψ'_h is evaluated by analysing a transversal cross-section (for radial flux motors) or rectified cylindrical sections (for axial flux motors) and by multiplying the corresponding unit length values by the active length l_m. The contribution ψ''_h is obtained by the analysis of longitudinal cross-sections (for radial flux motors) or radial sections (for the axial flux motors) and by multiplying the corresponding unit length values by the end-winding length. Since the end-winding effects involve leakage fluxes mainly flowing through the air, the corresponding inductances are very little affected by the current and θ, and can therefore be defined by means of one magnetostatic analysis [4].

5.3 Torque evaluation by single-phase supply

The torque in generic load conditions can be evaluated by elaborating values related to the single phase supply and to the null-current condition [4]. The single phase supply torque T^*_h is firstly determined, by considering the equivalent current i^*_h, according to (7), in order to take into account the actual magnetic saturation. Then, the cogging torque T_{emc} is evaluated by means of a sequence of null-current analyses and the residual phase torque $T^*_h-T_{emc}$ is multiplied by i_h/i^*_h to scale it to the actual current value. Finally, the resulting torque is:

$$T_{em}(\theta)=\sum_{h=1}^{3}\left[T_h^*(\theta_h,i_h^*)-T_{emc}(\theta_h)\right]\cdot\frac{i_h}{i_h^*}+T_{emc}(\theta) \quad (8)$$

where θ_h is the angular displacement between the h-phase and rotor reference axes (in particular $\theta_2=\theta$).

6 Examples of application

6.1 Parametric analysis

A steady-state operation is assumed at constant angular speed Ω=53.4 s^{-1} and 3-phase sinusoidal current supply is considered, with current density δ=8 A/mm^2. The corresponding coil ampereturns are given by $k_f h_c w_c \delta$ (k_f=0.7, fill-factor). The geometric constraints R_e=288 mm, L_{max}=170 mm e $R_{i,min}$=130 mm are assumed for all the configurations. The PM coercivity and remanence are set to $H_c=-8.9\cdot10^5$ A/m and B_r=1.23 T. The total permanent magnet volume V_m is fixed to 0.8 dm^3.

6.1.1 RFPM motor

The geometric quantities considered as design variables are the tooth angular amplitude $\alpha_t=w_t/R_g$, ($R_g=R_i+h_s+h_t+g/2$ mean air-gap radius), the PM length l_m, amplitude $\alpha_m=w_m/R_g$ and height h_m. The pole pitch number n_τ=24 corresponds to the number of PMs. The other geometrical parameters and the variation ranges for the design variables are shown in Table 1.

Table 1. Sizes and limits for the design variables (RFPM).

h_s= 20 mm	w_c= 13.6 mm	h_t= 39 mm
w_t= 32 mm	h_c= 31 mm	h_r= 20 mm
Δ_p= 12.9 mm	g= 3 mm	α_r= 15°, α_s= 20°
$h_{m,min}$= 8 mm	$\alpha_{m,min}$= 9.5°	$\alpha_{t,min}$= 7.15°
$h_{m,max}$=14 mm	$\alpha_{m,max}$= 11.5°	$\alpha_{t,max}$= 15.15°

A preliminary analysis has shown that the decrease of h_m (consistently with the geometric constraints and α_t, α_m being maintained) leads to the remarkable increase of the mean torque, because of the increase of l_m. In the further analyses, h_m is therefore set to 8 mm, minimum height to avoid the PM demagnetisation even with the peak short-circuit current. The variation of α_m and α_t involves the analysis of 25 configurations: $T_{em}(\theta)$ is calculated for each one according to (1) with n_h=2 harmonics; the corresponding torque ripple R_T and torque/mass ratios σ_i are evaluated by means of (2).
Some results of the analysis are reported in Table 2: it can be noticed that the ripple R_T is mainly affected by the magnet width and that the highest $\langle T_{em} \rangle$ value is achieved with a set $\{\alpha_t, \alpha_m\}$ for which both R_T and motor weight are high. According to (3), to obtain a good compromise among the different performance requirements, a performance index G is adopted, with χ_1=0.5, χ_2=0.1, χ_T=0.4, χ_k=0 for the rest of the terms.
The iso-value curves of G (Fig.8) show a fairly large region with better performances than the reference configuration (point P*), with the value of G in P about 13% lower than in P*. The comparison of $\langle T_{em} \rangle$ and R_T (Table 3) with the results of a 3D FEM code confirms that the 2D model gives satisfactory accuracy for the prediction of the RFPM motor performances.

Table 2. Some results of the parametric analysis (RFPM).

α_t [°]	α_m [°]	$\langle T_{em} \rangle$ [Nm]	R_T [%]	σ_T [Nm/kg]
7.15	9.5	1094.6	8.1	13.39
7.15	11.5	1005.7	4.6	14.45
11.15	9.5	1210.1	9.3	14.53
11.15	11.5	1109.5	3.7	15.65
15.15	9.5	1179.8	9.7	13.89
15.15	11.5	1080.3	3.4	14.94

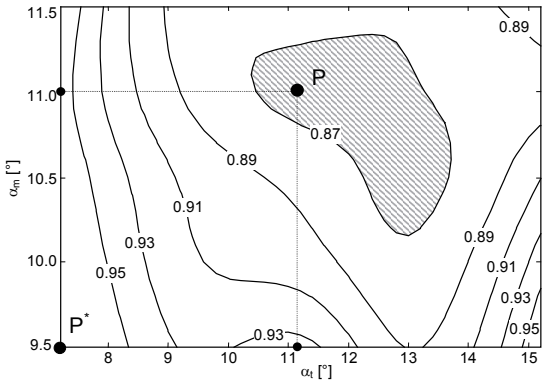

Fig.8. Iso-value curves of the index G; P*: reference point; P: optimal point (RFPM).

Table 3. Comparison between reference and optimal configurations (RFPM).

Quantity	Conf. P*		Conf. P	
	2D	3D	2D	3D
$\langle T_{em} \rangle$ [Nm]	1094	1075	1137	1094
R_T [%]	8.1	8.3	2.7	2.6
σ_T [Nm/kg]	13.39	13.16	15.45	14.86

6.1.2 AFPM-NS and AFPM-NN motors

The sizes of the AFPM motors are given in Table 4 (n_τ=24). A preliminary 2D analysis with α_m and h_m as variables and α_t constant has shown that the highest torque is achieved for the minimum magnet height able to avoid the PM demagnetisation. Set h_m to such value (8 mm), α_m and α_t are then assumed as design variables; the magnet radial size $l_m=(V_m/n_\tau)/(\alpha_m \cdot R_m \cdot h_m)$ is consequently constrained by the condition $0.67\alpha_r \leq \alpha_m \leq 0.9\alpha_r$, aimed to assure a clearance between adjacent magnets to make easier their placement on the rotor and to avoid excessive increasing of the overall radial size.

Table 4. Fixed sizes [mm] of AFPM-NS and NN motors.

Common sizes		AFPM-NS	AFPM-NN
R_m=247.5 mm	g= 3 mm	L= 142 mm	L= 146 mm
R_i=226 mm	α_s= 20°	h_t= 35 mm	h_t= 27 mm
h_r=15 mm	α_r= 15°	h_s=20 mm	h_s=40 mm
Δr=20 mm		w_c=12.7 mm	w_c=37.9 mm
		h_c=33 mm	h_c=22.2 mm

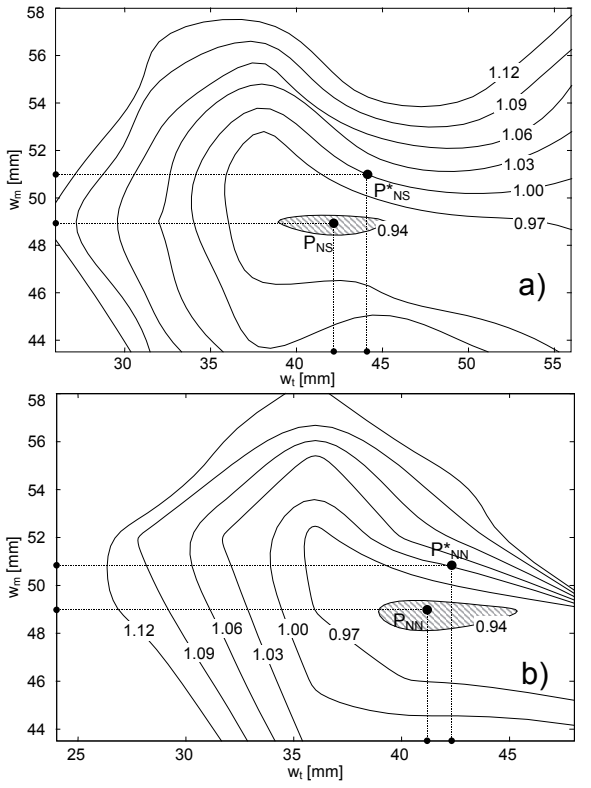

Fig.9: Iso-value curves of the index G for a) AFPM-NS (P^*_{NS}: reference point; P_{NS}: optimal point), b) AFPM-NN (P^*_{NN}: reference point; P_{NN}: optimal point).

Table 5. Comparison between reference and optimal configurations in AFPM motors.

Quant.	Conf. P^*_{NS}		Conf. P_{NS}		Conf. P^*_{NN}		Conf. P_{NN}	
	2D	3D	2D	3D	2D	3D	2D	3D
$\langle T_{em}\rangle$ [Nm]	1061	1059	1078	1080	1162	1158	1169	1158
R_T [%]	3.0	4.2	1.5	1.7	2.7	2.1	0.9	1.0
σ_T [Nm/kg]	12.33	12.31	12.66	12.69	12.30	12.26	13.01	12.89

The iso-value curves of G (Fig.9), (the values of χ_k are the same as in the RFPM analysis) allow to identify the optimal configurations (points P_{NS} and P_{NN}): with respect to the reference configurations (points P^*_{NS} and P^*_{NN}), R_T remarkably decreases, while $\langle T_{em}\rangle$ and σ_T slightly increase, as shown in Table 5; also in this case the comparison with the results of 3D FEM analyses confirms the effectiveness of the approach.

6.1.3 VHM motor

Indicated with N_s the number of stator poles and with N_m the number of PMs per pole, the number of rotor teeth N_r must be chosen according to the relation [22]:

$$N_r = N_m N_s/2 + k,\ k = N_s(i \pm 1/3),\ i = 1,2,3,... \qquad (9)$$

The number k of rotor teeth not faced to the stator pole should be as little as possible to maximize the stator-rotor interaction. The analysed configuration corresponds to the set $\{N_s, N_m, N_r\}=\{9, 6, 33\}$. The main geometric sizes, given in Table 6, are defined by a preliminary design and taking into account of both geometric and electromagnetic constraints: some important aspects to consider are the limitation of the rotor weight without increasing excessively the magnetic saturation especially in the rotor yoke and the achievement of a heavy vernier effect without reducing too much the air-gap length as well as avoiding the PMs demagnetization.

The influence of the rotor width w_t on $\langle T_{em}\rangle$ is investigated by means of the magnetic network approach (Fig.10). Even if $\langle T_{em}\rangle$ is overestimated (about 9%) with respect to the results of a 2D linear FEM analysis on a 120° motor sector, as for the dependence on w_t of its relative variation the results agree with the FEM ones: in fact, by decreasing w_t, a relative torque increase of about 27% is obtained in both the cases (with an absolute value of about 1550 Nm, according to the full model FEM analysis). A sequence of non-linear FEM analyses on the 3-pole model of the motor confirms the previous results.

Table 6. Sizes and limits of the design variables (VHM).

l_m = 80 mm	h_m=9 mm	R_i= 130 mm	R_r= 236.5 mm
g=2 mm	h_s= 35 mm	w_c= 21.3 mm	$w_{t,max}$=22.4 mm
h_t = 16 mm	h_c = 38 mm	$h_{r,min}$=25 mm	$w_{t,min}$=12.8 mm
w_p= 60 mm		$h_{r,max}$=35 mm	$\tau=w_m$=22.4 mm

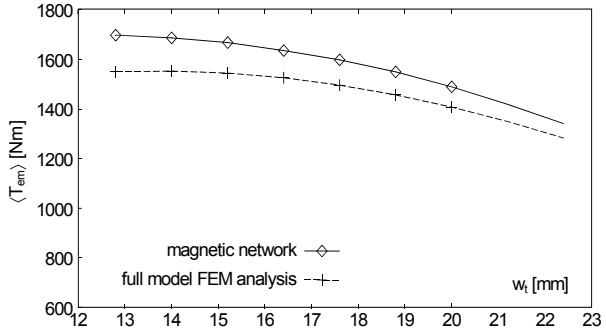

Fig.10. Mean torque $\langle T_{em}\rangle$ as function of w_t (VHM).

Table 7. Comparison between the initial and the improved configuration (VHM).

Conf.	$\langle T_{em}\rangle$ [Nm]	R_T [%]	m_{pm} [kg]	m_s [kg]	m_r [kg]	σ_T [Nm/kg]
A	1082.3	4.7	6.6	68.9	44.2	9.57
B	1423.0	2.7	6.9	71.1	31.1	13.92

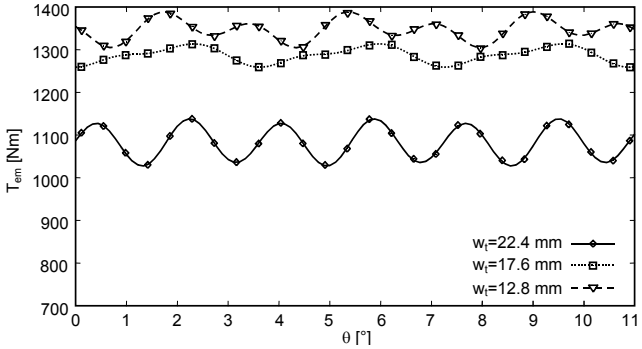

Fig.11. Torque as function of rotor position for different tooth width (VHM).

The ripple R_T (evaluated by (1) and (2), with $n_\tau=N_r$ and n_h=3) has a minimum (≈1.9%) for the tooth width value w_t'=17.6 mm (Fig. 11). As for other geometric parameters, the analysis shows the rotor tooth height h_t slightly affects the torque, while the reduction of rotor yoke height improves $\langle T_{em}\rangle$ (up to +7%) but worsens the torque ripple R_T.

The relevant quantities related to the initial and improved configurations (A and B, respectively) corresponding to the sets $\{w_{t,max},h_{r,max}\}$ and $\{w_t',h_{r,min}\}$ are compared in Table 7. It's worth to remark the improvement of $\langle T_{em}\rangle$ (≈+30%) and σ_T (≈+45%) in B, mainly thanks to the adjustment of the tooth width.

6.2 Dynamical model

The performance of a TFPM motor with n_τ=24 poles (main sizes in Table 8, [19]) is analysed by means of the single-phase supply methodology described in 5.1. The phases consist of six branches in parallel, each composed of two series-connected coils with 110 turns wound around the same core. The electromagnetic parameters, calculated by means of 3D FEM analyses

for n_r=16 rotor positions and n_i=13 values of the coil current in the range –60÷60 A, make possible the definition of the interpolating function to be applied for the analysis of the motor operation under different supplying strategies. The results are compared with 3-phase FEM simulations, related to both current and voltage source supply.

A quadrature condition between PM and armature fields is assumed in the former case: the torque profile show good correspondence between the proposed method and the 3-phase supply FEM simulation (Fig.12). The good agreement is confirmed in the latter case by the steady-state current waveforms (Fig.13). It's worth to point out that the 3-phase supply simulation by means of a FEM transient code requires no less than 35 hours on a ordinary PC, while the proposed method takes about 30 minutes for the solution on the same PC. Since about 60 hours are necessary to determine the mathematical model, the proposed procedure is convenient whenever several operating conditions have to be analyzed.

Table 8. Sizes of the TFPM motor.

L= 142 mm	R_i =147 mm	g = 3 mm	ΔR = 20 mm
d_0 = 5 mm	d_c = 6.6 mm	w_c = 12.7 mm	h_c = 33 mm
w_m = 53 mm	h_m = 8 mm	w_s = 33 mm	l_t = 42 mm
h_r = 10 mm	β = 45°	α_s= 20°	α_r= 15°

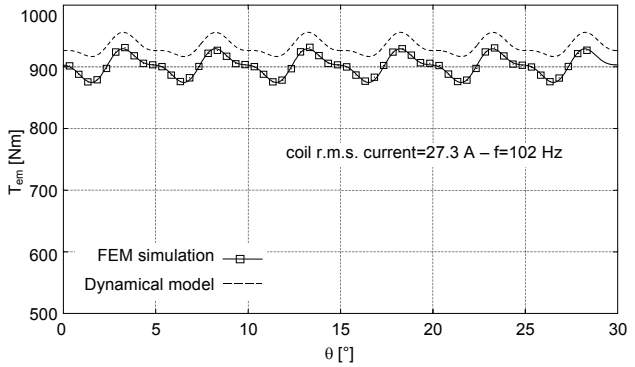

Fig.12. Electromagnetic torque with current source supply (TFPM).

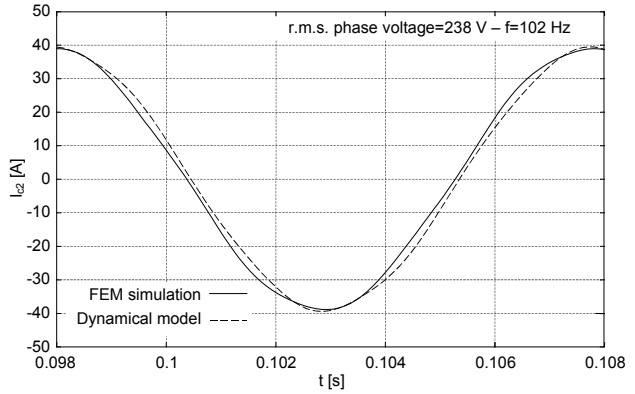

Fig.13. Coil current waveform with voltage source supply (TFPM).

7 Conclusions

The complexity of the in-wheel PM motor electromagnetic design, due to both the geometric configuration and the saturation effects, generally requires FEM-based codes to evaluate the motor performances with acceptable accuracy. However, their application may result in remarkable calculation times and in troublesome management of the design procedures.

The general methodology proposed in the paper allows to simplify the analysis of several motor topologies, in both steady-state and transient operating conditions. In particular the adoption of suitable 2D simplified models and the reduction of the state variables allow to implement flexible and fast calculation procedures useful in the preliminary design and in the electromagnetic optimization. The examples of application show the effectiveness of the proposed procedures to evaluate and to improve the motor performances complying with the design constraints. The results are validated by the comparison with FEM 3D and transient codes.

8 References

[1] G.H. Chen, K.J. Tseng, ″Design of a permanent-magnet direct-driven wheel motor drive for electric vehicles", *Proc. of IEEE PESC'96,* pp.1933-1939, Baveno, Italy, 23-27 June 1996.

[2] C. Espanet, A. Miraoui, J.M. Kauffmann, ″Optimal Design of an High Torque DC Brushless In-Wheel Motor″, *Proc. of IEEE IEMDC'03*, Vol.3, pp.1402-1409, 1-4 June 2003

[3] S. Brisset, G. Odoux, P. Brochet, ″Brushless DC Wheel Motor for Electric Vehicle″, *Proc.of EVS18*, Berlin, Germany, 20-24 October 2001.

[4] M. Andriollo, G. Bettanini, G. Martinelli, A. Morini, A. Tortella, ″Design and Analysis of a SPM In-Wheel motor for the propulsion of electric buses″, *Proc. of Electromotion 2005,* Lausanne, Switzerland, 27-29 September 2005.

[5] F. Caricchi, F. Crescimbini, F. Mezzetti, E. Santini ″Multi axial flux PM machine for wheel direct drive″, *IEEE Trans. on Industry Applications*, vol.32, n.4, pp.882-888, July/August 1996.

[6] F. Profumo, Z. Zhang, A. Tenconi, ″Axial flux machine drives: a new viable solution for electric cars″, *Proc. of IECON 1996*, Vol.1, pp.34-40, Taipei, Taiwan, 5-10 August 1996

[7] F. Caricchi, F. Crescimbini, O. Honorati, A. Di Napoli, E. Santini, ″Compact wheel direct drive for EVs″, *IEEE Industry Applications Magazine*, pp.25-32, November/December 1996.

[8] S. Huang, J. Luo, F. Leonardi, T.A. Lipo, ″A Comparison of Power Density for Axial Flux

Machines Based on General Purpose Sizing Equations", *IEEE Trans. on Energy Conversion,* Vol.14, n.2, pp.185-192, June 1999.

[9] A. Cavagnino, F. Profumo, A. Tenconi, "Axial Flux Machines: Structures and Applications", *Proc. of Electromotion 2001*, Bologna, Italy, 19-20 June 2001.

[10] M. Aydin, S. Huang, T.A. Lipo, "Design and Electromagnetic Field Analysis of non slotted and slotted TORUS type Axial Flux Surface Mounted Disc Machines", *Proc. of IEEE IEMDC'01,* Boston, USA, 17-20 June 2001.

[11] S. Huang, M. Aydin, T.A. Lipo, "Low Noise and Smooth Torque Permanent Magnet Propulsion Motors: Comparison of Non-slotted and Slotted Radial and Axial Flux Topologies", *Proc. of IEEE ACEMP'01,* pp.1-8, Kusadasi, Turkey, 27-29 June 2001 (Invited Paper).

[12] M. Aydin, S. Huang, T.A. Lipo, "Optimum Design and 3D Finite Element Analysis of Non-slotted and Slotted Internal Rotor Type Axial Flux PM Disc Machines.", *Proc. of IEEE PES'01 Summer Meeting,* Vol.3, pp.1409-1416, Vancouver, Canada, 15-19 July 2001.

[13] M. Aydin S. Huang, T.A. Lipo, "Torque Quality and Comparison of Internal and External Rotor Axial Flux Surface-Magnet Disc machines", *Proc. of IECON'01,* Denver, USA, 29 November-2 December 2001.

[14] S. Huang, M. Aydin, T.A. Lipo, "TORUS Concept Machines: Pre-Prototyping Assessment for Two Major Topologies", *Proc. of IEEE-IAS Annual Meeting,* pp.1619-1625, Chicago, USA, 30 September-5 October 2001.

[15] A M. Cirani, C. Sadarangani, P. Thelin, "Analysis of an innovative design for an axial flux Torus machine", *Proc. of ICEM 2002,* pp.202-207, Bruges, Belgium, 25-28 August 2002.

[16] M. Aydin, S. Huang, T.A. Lipo, "Axial Flux Permanent Magnet Disc Machines, a Review", *Proc. of SPEEDAM 2004,* Capri, Italy, 16-18 June 2004.

[17] R. Blissenbach, G. Henneberger, U. Schaefer, W. Hackmann, "Development of a Transverse Flux Traction Motor in a Direct Drive System", *Proc. of ICEM 2000,* Espoo, Finland, 28-30 August 2000.

[18] M. Andriollo, G. Martinelli, A. Morini, A. Tortella, M. Zerbetto, "A Transverse Flux Wheel Hub Motor for Electric Buses", *Proc. of SPEEDAM 2004,* Capri, Italy, 16-18 June 2004.

[19] M. Andriollo, M. Forzan, G. Martinelli, A. Morini, A. Tortella, M. Zerbetto, "Performance Analysis of a Transverse Flux Wheel Motor by a Non-linear Mathematical Model", *Proc. of ICEM 2004,* Cracow, Poland, 5-8 September 2004.

[20] M.A. Mueller, N.J. Baker, "Modelling the Performance. of the Vernier Hybrid Machine", *IEE Proc. Part B, Elec. Power Appl*., Vol. 150, n.6, pp.649-654, November 2003.

[21] E. Spooner, L. Haydock, "Vernier Hybrid Machines", *IEE Proc. Part B, Elec. Power Appl*., Vol.150, n.6, pp.655-662, November 2003.

[22] M. Andriollo, G. Bettanini, G. Martinelli, A. Morini, A. Tortella, "Performance Analysis of an In-Wheel Vernier Hybrid Motor for Electric Propulsion", *Proc. of Electromotion 2005,* Lausanne, Switzerland, 27-29 September 2005.

[23] C. Espanet, M. Tekin, R. Bernard, A. Miraoui, J.M. Kauffmann, "A New Structure of an High Torque In-wheel Motor", *Proc. of ICEMS 2003*, Vol.1, pp.158-162, Beijing, China, 8-11 November 2003.

[24] A. Lange, W.R. Canders, F. Laube, H. Mosebach, "Comparison of different drive system for a 75 kW eletrical vehicle drive", *Proc. of ICEM 2000,* Espoo, Finland, 28-30 August 2000.

[25] K. Sitapati, R. Krishnan, "Performance Comparison of Radial and Axial Field Permanent Magnet Brushless Machines", *IEEE Trans. on Industry Applications*, Vol.37, n.5, September/October 2001.

[26] S. Huang, M. Aydin, T.A. Lipo, "Torque quality assessment and sizing optimisation for surface mounted PM machines", *Proc. of IEEE IAS 2001 Annual Meeting*, Chicago, USA, 30 September-4 October 2001.

[27] A. Cavagnino, M. Lazzari, F. Profumo, A. Tenconi, "A Comparison between the Axial Flux and the Radial Flux Structures for PM Synchronous Motors", *IEEE Trans. on Industry Applications*, Vol.38, n.6, November/December 2002.

[28] Z. Rahman, "Evaluating radial, axial and transverse flux topologies for in-wheel motor", *Power Electronics in Transportation,* pp.75-81, October 2004.

[29] K. Rahman, N. Patel, T. Ward, J. Nagashima, F. Caricchi, F. Crescimbini, "Application of Direct Drive Wheel Motor for Fuel Cell Electric and Hybrid Electric Vehicle Propulsion System", *Proc. of IEEE IAS 2004 Annual Meeting,* Vol.3, pp.1420-6, Seattle, USA, 3-7 October 2004.